RSC Advances

PAPER

View Article Online
View Journal | View Issue

Check for updates

Cite this: *RSC Adv.*, 2023, **13**, 34693

Designing an efficient lead-free perovskite solar cell with green-synthesized $CuCrO_2$ and CeO_2 as carrier transport materials

Sagar Bhattarai, *[a] Dharitri Borah,[b] Jayashree Rout,[c] Rahul Pandey, *[d] Jaya Madan,*[d] Ismail Hossain,[e] Palky Handique,[f] Mohd Zahid Ansari, *[g] M. Khalid Hossain *[h] and Md. Ferdous Rahman *[i]

With increased efficiency, simplicity in manufacturing, adaptability, and flexibility, solar cells constructed from organic metal halide perovskite (PVK) have recently attained great eminence. Lead, a poisonous substance, present in a conventional PVK impacts the environment and prevents commercialization. To deal with this issue, a number of toxicity-free PVK-constructed solar cells have been suggested. Nevertheless, inherent losses mean the efficiency conversion accomplished from these devices is inadequate. Therefore, a thorough theoretical investigation is indispensable for comprehending the losses to improve efficiency. The findings of a unique modelling method for organic lead-free solar cells, namely methylammonium tin iodide ($MASnI_3$), are investigated to reach the maximum practical efficiencies. The layer pertinent to $MASnI_3$ was constructed as a sandwich between a bio-synthesized electron transport layer (ETL) of CeO_2 and a hole transport layer (HTL) of $CuCrO_2$ in the designed perovskite solar cells (PSCs). In this study, the use of algae-synthesized Au in the back contacts has been proposed. To obtain the maximum performance, the devices are further analyzed and optimized for active layer thickness, working temperature, total and interface defect density analysis, impedance analysis (Z'–Z), and capacitance–voltage (C–V), respectively. An optimal conversion efficiency of 26.60% has been attained for an $MASnI_3$-constructed PSC. The study findings may open the door to a lead-free PSC through improved conversion efficiencies.

Received 3rd October 2023
Accepted 20th November 2023

DOI: 10.1039/d3ra06722j

rsc.li/rsc-advances

Open Access Article. Published on 28 November 2023. Downloaded on 11/13/2024 4:18:44 PM.
This article is licensed under a Creative Commons Attribution-NonCommercial 3.0 Unported Licence.

1. Introduction

The primary research goal for the decade is the overall augmentation of power conversion efficiency (PCE) of non-toxic, renewable solar cells, as a replacement for conventional fuels. Perovskite solar cells (PSCs) in particular have attracted great interest because of their remarkable qualities, including their extremely high coefficient of absorption, low cost, long charge diffusion length, great electron mobility, low trap state density, low binding energy of excitons, and configurable band gaps.[1–5]

A perovskite material has an archetypical structure relating to ABX_3, where A is likely to be a methylammonium cation ($CH_3NH_3^+$). A has a very small ionic radius of ~0.18 nm. B is often Pb or Sn, while X is characteristically a halide.[6–8] It should be mentioned that Kojima *et al.* introduced a noble PSC structure, where $CH_3NH_3PbX_3$ and Br were used to build the active layer as a halide material, which presented a recorded PCE of up to 3.8%.[9] Thenceforth, remarkable progress have been achieved in PSC performance over recent years, but there is still a lot of room for improvement. Suitable material selection with optimum thickness, defectivity, and adequate working temperature in device architectures is critical in improving device effectiveness.

A PSC sustains a lower photocurrent density because of a characteristically thin active layer absorbing markedly low quantities of photons. Interestingly, as the thickness of the perovskite active layer increases, less charge extraction is

[a]*Technology Innovation and Development Foundation, Indian Institute of Technology Guwahati, Guwahati 781039, Assam, India. E-mail: sagarbhattarai012@gmail.com*
[b]*Department of Environmental Science, Arunachal University of Studies, Namsai, 792103, Arunachal Pradesh, India*
[c]*Department of Ecology and Environmental Science, Assam University, Silchar, 780011, Assam, India*
[d]*VLSI Centre of Excellence, Chitkara University Institute of Engineering and Technology, Chitkara University, Punjab, India. E-mail: rahul.pandey@chitkara.edu.in; jaya.madan@chitkara.edu.in*
[e]*School of Natural Sciences and Mathematics, Ural Federal University, Yekaterinburg 620000, Russia*
[f]*Department of Mathematics, Arunachal University of Studies, Namsai, 792103, Arunachal Pradesh, India*
[g]*School of Materials Science and Engineering, Yeungnam University, 280 Daehak-Ro, Gyeongsan, Gyeongbuk 38541, Republic of Korea. E-mail: zahid.smr@yu.ac.kr*
[h]*Institute of Electronics, Atomic Energy Research Establishment, Bangladesh Atomic Energy Commission, Dhaka 1349, Bangladesh. E-mail: khalid.baec@gmail.com*
[i]*Advanced Energy Materials and Solar Cell Research Laboratory, Department of Electrical and Electronic Engineering, Begum Rokeya University, Rangpur 5400, Bangladesh. E-mail: ferdousapee@gmail.com*

© 2023 The Author(s). Published by the Royal Society of Chemistry

Open Access Article. Published on 28 November 2023. Downloaded on 11/13/2024 4:18:44 PM.
This article is licensed under a Creative Commons Attribution-NonCommercial 3.0 Unported Licence.

observed in the device output. Also, reasonable recombination-related loss is observed with increased active layer thickness.[8,10] So, selecting a suitable thickness becomes a primary concern amongst others in PSC devices.

Apart from the instability involved, the influence of electrode degradation on perovskite solar cells has also been studied.[11] Their stability with Au and Ag as the electrodes in a triple-cation $MAPbI_3$-based PSC were also tested.[12] In another study, it can be seen that the degradation of a lead halide PSC was greatly influenced by the hole transport layer and the effect of the metal electrode interfaces was also revealed.[13] So, stability based on the electrodes in the PSC design has been studied thoroughly in the reports discussions above.

The perovskite layer is held in a sandwich between the electron (ETL) and hole carrier transport layers (CTLs) in classic PSC architecture (ETL and HTL). Spiro-OMeTAD was used in HTL to maximize effectiveness and stability.[14] Concurrently, Liu *et al.* improved the efficiency of a complex device structure, with an ITO/TiO_2/$CH_3NH_3PbI_{3-x}Cl_x$/Spiro-OMeTAD/Ag layer structure, by 15.4% by employing contemporary vapour deposition approaches.[15] But, due to cost, the Spiro-OMeTAD application is impractical to use, a significant concern in PSC manufacturing.[8] To replace this complex structure, we employ similar characteristics of the HTL material $CuCrO_2$ for application in PSC devices. Similarly, TiO_2 offers relatively low impacts on charge transportation to the anode; it has a non-matching bandgap with the active layer. Moreover, a green-synthesis approach makes the material economical for perovskite fabrication. Recently, efficiency with reference to a PSC was increased by using CeO_2 as an ETL and an annealing treatment, increasing efficiency up to 18.36%.[16] Butt *et al.*, synthesized CeO_2 nanoparticles (NPs), from petals, a plausible material for ETL in present devices. It is important to highlight that planar heterojunction PSCs are workable substitutes for mesoscopic designs because of their simplicity and ease of production.[17,18]

Applications of 'green-synthesized nanomaterials' from microbes (algae/bacteria//actinomycetes/fungi) and plants in modern science and technology have come to the fore thanks to their sustainability, cost-effectiveness, and low toxicity, together with their eco-friendly properties. United Nations 'Sustainable development Goal'-7 is directly related to affordability together with clean energy. Applying green-synthesized materials in solar cells with the required photovoltaic parameters will provide clean energy with greater efficiency and affordable cost, achieve economic growth, and alleviate climate change.

The 'CeO_2-NPs' were prepared from the flowers of *Cassia glauca*.[19] The dried petals (20 g) of the flowers were extracted in dH_2O (200 mL) and filtered. The extract (100 mL) was pre-heated (75 °C) with stirring (1000 rpm). The extract was alkylated [pH 9; NaOH (0.1 M)]. $Ce(NO_3)_3 \cdot 6H_2O$ (5 g) was added to the extract, heated (75 ± 5 °C), stirred (1000 rpm), and finally centrifuged to collect the NPs. The CeO_2-NPs were spherical, presenting a lattice constant of 5.42 Å, and a 'crystallite size' of 3.20 nm. The delafossite ($CuCrO_2$) was prepared from chelating/complexing *Aloe vera* extracts,[20] where 15 g of dried plant in 100 mL of dH_2O was stirred for 1 h (60 °C). Millimole equivalents of both $Cu(NO_3)_2 \cdot 3H_2O$ (0.241 g) and $Cr(NO_3)_3 \cdot 9H_2O$ (0.40

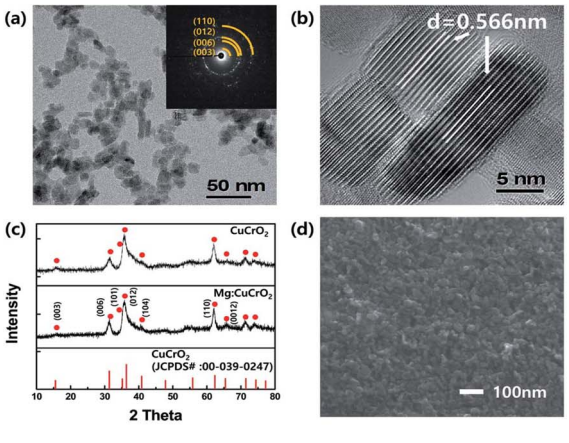

(i)

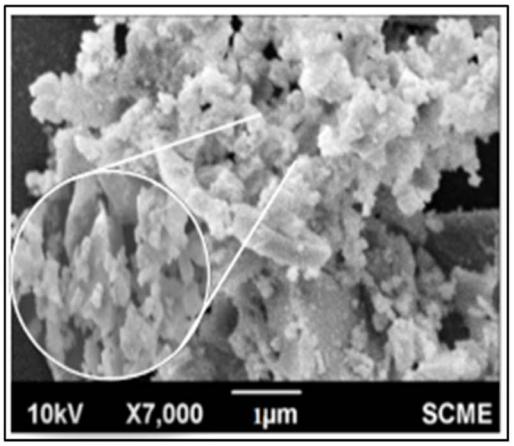

(ii)

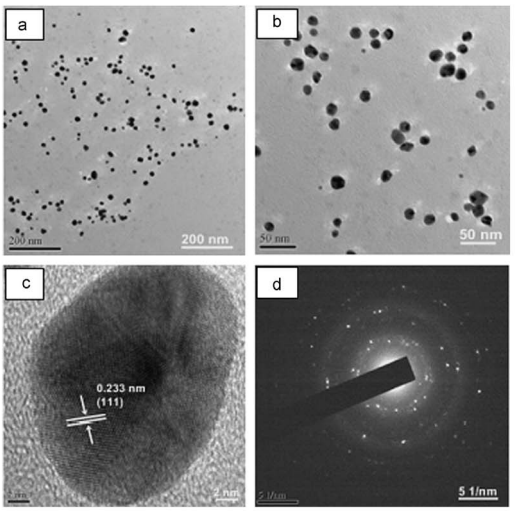

(iii)

Fig. 1 The green-synthesized (i) $CuCrO_2$ morphology for use as HTL (from *Aloe barbadensis*);[33] (ii) the morphology of CeO_2 (from petals of *Cassia glauca*) (reprinted with permission from ref. 19). (iii) Au-nanoparticle (from *Prasiola crispa*) as a back contact of the $MASnI_3$-based PSC devices (reprinted with permission from ref. 21).

© 2023 The Author(s). Published by the Royal Society of Chemistry

Open Access Article. Published on 28 November 2023. Downloaded on 11/13/2024 4:18:44 PM.
This article is licensed under a Creative Commons Attribution-NonCommercial 3.0 Unported Licence.

g) were separately added to 100 mL of extract, mixed, and heated (80 °C) until a clear solution appeared. The solution was further heated (100–120 °C) to a gelatinous mass, dried completely (150 °C, 12 h), and calcined (500 °C, 6 h).

'Au-NPs' were synthesized from *Prasiola crispa*, an epilithic alga, by bioreduction.[21] Briefly, 1 g of dry powder of the alga in $HAuCl_4$ solution (10^{-3} M, 100 mL) was stirred until the colour changed to purple (12 h). The NPs presented an approximately spherical shape (5–25 nm), a crystallite size of 9.8 nm, lattice fringes of 0.233 nm, and polycrystalline nature. A 'dynamic light scattering' study revealed the average diameter to be 10 ± 8.6 nm.

A significant advancement in Pb-based PVK materials has occurred in the last few decades. However, the toxicity of lead remains a primary barrier to the broad adoption of PSCs.[22] These issues can be overcome by substituting Sn for Pb, which is toxic-free in nature.[23–25] Moreover, $MASnI_3$ material has certain advantages pertaining to its bandgap (~1.3 eV), which is remarkably smaller than that of a conventional PVK material.[26] Its reduced bandgap might be the reason for photon absorption by $MASnI_3$ over a wide spectrum of wavelengths. A wider photon wavelength absorption and narrower bandgap enhance device efficiency (from 1.3 eV). The optimization of defect-less, light-harvesting layers to obtain desired optoelectronic characteristics has more impact on the output of a PSC device.

In the present work, SCAPS-1D, a (1-dimensional) simulator of solar cell capacitance, developed by ELIS, University of Ghent, Belgium was used for investigation of the associated PSC, developed with a drift-diffusion model.[27] The advantages of the simulator include a deposition capability pertaining to a maximum of seven semiconducting layers together with the ability to rank virtually all characteristics. The mechanism involves the solving of the Poisson equation besides continuity equations, and the simulations may be done under both dark and light conditions.[28] The above-mentioned simulator is also convenient for analysing various models with recombination mechanisms, batch computation with the bulk, and interface defect-level calculation.[29] The current simulation is applied to both crystalline and amorphous solar cells.[30] The present work applies AM1.5G solar irradiance relating to an analysis of carrier transport processes and electrical outputs for the construction of an optical profile, which could be converted into an electrical model for $MASnI_3$-based PSCs.

2. Simulated device structures

As an innovative approach to the advancement of the device, we propose the previous work by Sarkar *et al.* to find the HTL of $CuCrO_2$ and CeO_2 as the ETL as reported by Butt *et al.* (see Fig. 1(i–iii)).[19,20] Similarly, the algae-synthesised Au is used as a back contact for the PSC, as shown below. We designed the structure of ITO/CeO_2/$MASnI_3$/$CuCrO_2$/Au (Fig. 2(i)). The green-synthesized ETL and HTL were implemented in a PSC device, as shown in Fig. 2. The ITO top electrode (0.1 μm) is followed by a CeO_2 layer (0.1 μm) in the simulated PSC devices, which is a green-synthesized ETL (Fig. 1). In the architecture of the PSC, the electrons produced are effectively collected from the absorber layers. The absorber layer of the device has a thickness of 0.6 μm and is preserved between an ETL and the HTL. The cathode efficiently receives a hole from PVK thanks to the hopping mechanism. $CuCrO_2$ with a thickness of 0.1 μm was also green-synthesized (Table 1). The designed layers were initially as depicted in Table 1. Using the ETL (CeO_2) and HTL ($CuCrO_2$) results in better alignment with the perovskite material. Apart from the band alignment, both bio-synthesised materials have suitable carrier mobility. The cathode is made of Au, an algae-synthesized material of 0.1 μm thickness. Whereas in Fig. 2(ii), the absorption coefficient of the $MASnI_3$ material is depicted from SCAPS-1D. The modelling-related attributes in PSC devices are listed in detail in Table 1.

3. Mathematical modeling

The Solar Cell Capacitance Simulator, SCAPS-1D, allows for numerical modelling of the key parameters influencing the output of a PSC device.[27] Considering steady-state conditions, the semiconductor materials are governed by a one-dimensional equation. The charge density of the p–n

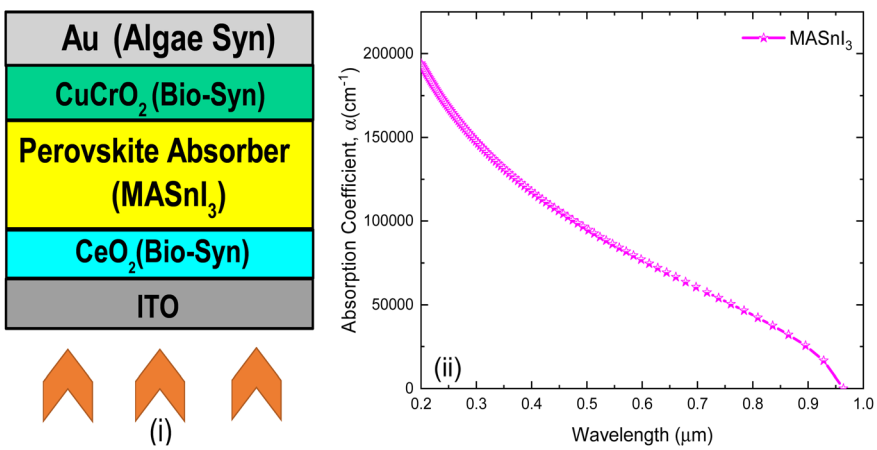

Fig. 2 (i) Simulated architecture of $MASnI_3$-based PSC devices, and (ii) absorption coefficient of $MASnI_3$ material under AM1.5G illuminance.

Open Access Article. Published on 28 November 2023. Downloaded on 11/13/2024 4:18:44 PM.
This article is licensed under a Creative Commons Attribution-NonCommercial 3.0 Unported Licence.

Table 1 The simulated inputs in the architecture of the PSC device[20,31,32]

Parameters	Terms	ETL (CeO_2)	PVK ($MASnI_3$)	HTL ($CuCrO_2$)
d (μm)	Thickness	0.1–0.15	0.1–0.9	0.1–0.15
E_g (eV)	Bandgap	3.2	1.3	3.0
ε_r	Relative permittivity	9	8.2	9.5
χ (eV)	Electron affinity	4.4	4.1	2.1
N_c (cm^{-3})	Effective DoS at CB	1×10^{20}	2×10^{18}	1×10^{19}
N_v (cm^{-3})	Effective DoS at VB	2×10^{21}	2×10^{18}	1×10^{19}
μ_n ($cm^2\ V^{-1}\ s^{-1}$)	Mob. of electrons	100	1.6	0.1
μ_p ($cm^2\ V^{-1}\ s^{-1}$)	Mob. of holes	25	1.6	2.53
D_a (cm^{-3})	Dop. conc. of the acceptor	0	0	6.4×10^{15}
D_d (cm^{-3})	Dop. conc. of donor	1×10^{21}	1×10^{19}	0
N_t (cm^{-3})	Defect density	1×10^{14}	1×10^{14}	1×10^{14}

junction, and its relationship with the electric field (E), can be depicted using the following symbols:

$$\frac{\partial^2\varphi}{\partial^2 x} = -\frac{\partial E}{\partial x} = -\frac{\rho}{\varepsilon_s} = -\frac{q}{\varepsilon_s}\left[\mathrm{p} - \mathrm{n} + N_D^+(x) - N_A^-(x) \pm N_{def}(x)\right] \quad (1)$$

Here φ is electrostatic potential; q is charge; ε_s is static relative permittivity for the medium; n and p are electron and hole, respectively; N_D and N_A are donor and acceptor densities; and N_{def} is defect density for the acceptor and donor.

In the PSC device, the equation for carrier continuity was followed:[34]

$$-\frac{\partial j_p}{\partial x} + G - U_p(\mathrm{n},\mathrm{p}) = 0 \quad (2)$$

$$\frac{\partial j_n}{\partial x} + G - U_n(\mathrm{n},\mathrm{p}) = 0 \quad (3)$$

where j_p and j_n are the current densities of the hole and electron; G is the carrier generation rate; and U_n(n, p) is the recombination rate pertinent to the electron and hole.

Simultaneously, the carrier current density was ascertained from the equations:[35]

$$j_p = qn\mu_p E - qD_p\frac{\partial \mathrm{p}}{\partial x} \quad (4)$$

$$j_n = qn\mu_n E + qD_n\frac{\partial \mathrm{n}}{\partial x} \quad (5)$$

Here q is charge; μ_p and μ_n are carrier mobilities; and D_p D_n are the diffusion coefficients of the carriers.

The basic equation pertaining to solar cells (current density, generation and recombination rate) was extracted from the SCAPS-1D software.

4. Results and discussion

An extensive examination together with an analysis pertaining to intrinsic solar cell parameters is presented in subsections 4.1 to 4.9.

4.1 Alignment of the bandgaps of the PSC structure

The band diagram encompassing the simulated device (PSC) at equilibrium is presented in Fig. 3 to understand the carrier dynamics within the device. The first $MASnI_3$-constructed PSC device presents an energy barrier (0.02 eV) between the TiO_2 conduction band minimum (E_C) and the lowest unoccupied molecular orbital (LUMO) in the absorber material with an offset of around 1.85 eV between the HOMO and HTL. For an $MASnI_3$-constructed PSC, rapid electron transport can be shown; see below. The details are depicted in Fig. 3 with ETL, HTL, and perovskite thickness.

4.2 The impact of active layer thickness, ETL and HTL on PSC output

A predetermined extension applying to the preconditioned input parameters at 300 K was applied to complete the thorough simulation analysis (Table 1). Further, to understand the performance of the device with variation in absorber layer thickness, the PV parameters were obtained and are reported in Fig. 4. The effect associated with active layer thickness with reference to the output attributes of the $MASnI_3$-based PSCs has been confirmed in Fig. 4. As the thickness of the perovskite absorbing layer (PAL) in the device grows, the short circuit current density (J_{SC}), open circuit voltage (V_{OC}), and power conversion efficiency (PCE%) rise to achieve a saturated value

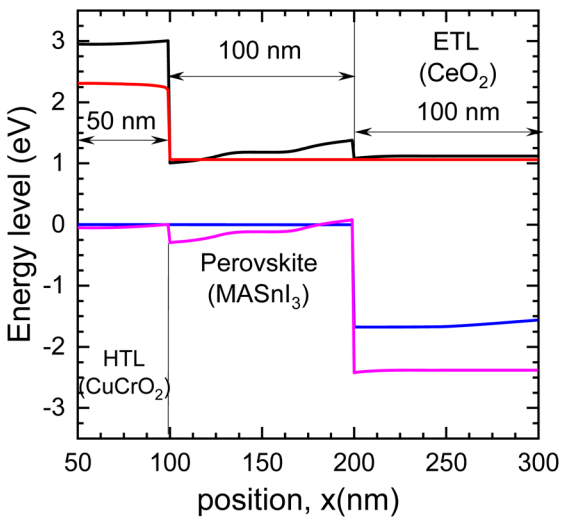

Fig. 3 The energy band diagrams ascribed to an $MASnI_3$-based PSC device with designed ETL and HTL.

© 2023 The Author(s). Published by the Royal Society of Chemistry

Open Access Article. Published on 28 November 2023. Downloaded on 11/13/2024 4:18:44 PM.
This article is licensed under a Creative Commons Attribution-NonCommercial 3.0 Unported Licence.

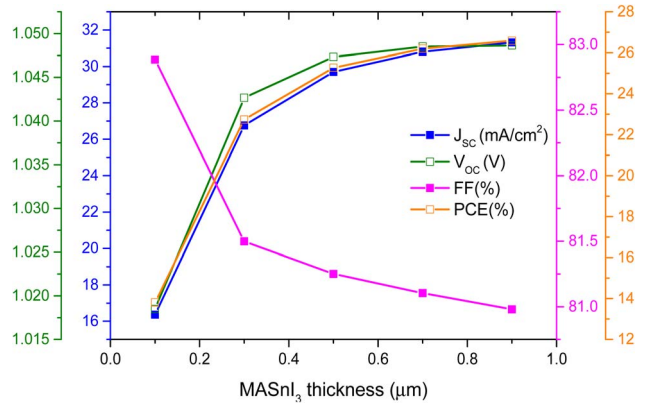

Fig. 4 The effect of the thickness of the $MASnI_3$ layer on the PV parameters of the designed PSC device.

(31.31 mA cm^{-2}) at 0.9 μm (Fig. 4). It should be highlighted that a rise in the generation rate of excitons occurred with greater absorbance in the absorber layers with PAL thickness of 0.9 μm. Additionally, the FF of the device falls monotonically as the thickness increases because a small increase in thickness increases carrier recombination.

The J_{SC}, V_{OC}, FF and PCE at different thicknesses of $CuCrO_2$ and CeO_2 are presented in Fig. 5 and 6, respectively, to understand the impact of variation in HTL and ETL layer thickness. The parameters achieved a maximum value with thicknesses of 100 nm each of $CuCrO_2$ and CeO_2. Previous work by Bhattarai *et al.* also shows that the optimized ETL and HTL thickness is 100 nm.[36] It achieves larger values for J_{SC} (31.31 mA cm^{-2}), V_{OC} (~1.05 V), FF (80.98%) and PCE (26.60%). This might be because of the lack of contribution to photon absorption in a PSC.[22]

4.3 The impact of temperature on PSC parameters

A complete analysis pertaining to solar cell properties with variation in temperature is presented in Fig. 7. The four parameters, J_{SC}, V_{OC}, FF, and PCE, all drop as the temperature rises from 300 to 375 K, relating to the degradation of the materials. For the $MASnI_3$-based PSC devices, J_{SC} was

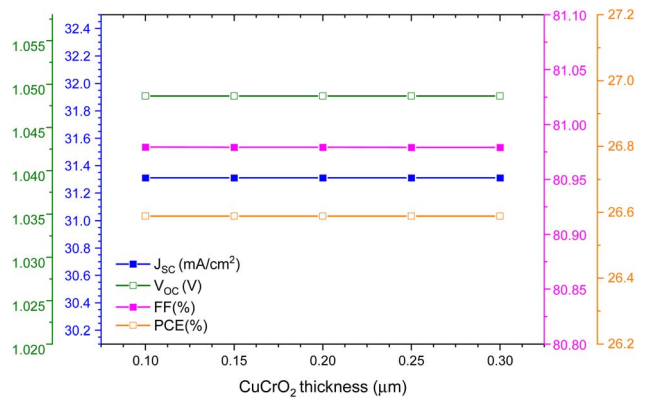

Fig. 5 The effect of the thickness of the $CuCrO_2$ layer on the PV parameters of the designed PSC device.

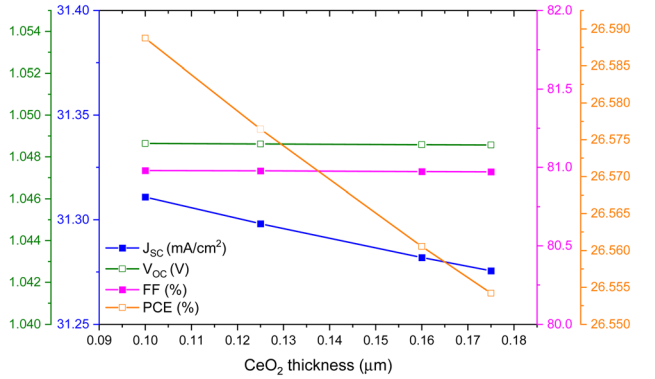

Fig. 6 The effect of the thickness of the CeO_2 layer on the PV parameters of the designed PSC device.

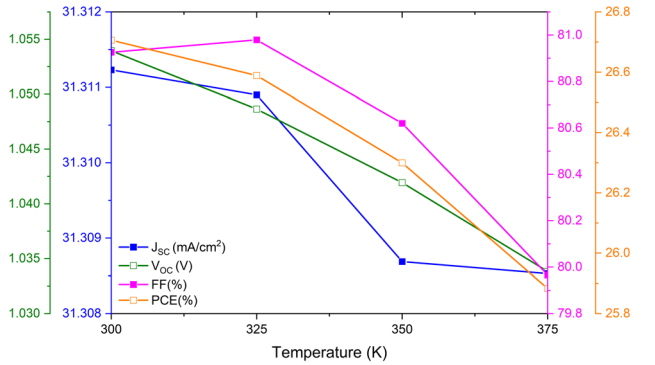

Fig. 7 The effect of temperature on the solar cell PV output parameters in the PSC.

a maximum at 300 K (31.31 mA cm^{-2}). These values may be appropriate for the device output characteristics. Due to internal degradation of the PVK material, V_{OC} continues to degrade and exhibits a higher value at 300 K (1.05 at 300 K dropping to 1.034 V at 375 K). Similarly, FF value decrease from 80.5% to 79.55% as the temperature increases from 300 K to 375 K. The PCE (26.65% at 300 K) degrades to 25.9% at a temperature of 375 K.

4.4 The impact of defect density and thickness on the parameters of the PSC

The previous subsection concerning the thickness of the fixed absorber layer with reference to the PSC device looked solely into the effects of bulk defect density on performance metrics, as reported in Fig. 8. However, varied fault concentrations at disparate thicknesses of absorber layers help us to comprehend device performance with reference to the combined variations in defect and thickness. Therefore, the collective variation is obtained in a separate subsection. Determining the impact of defect density on PSC performance as a whole is the foremost goal of a study on defect density. Initially, defect density was raised to 1×10^{16} cm^{-3} from 1×10^{14} cm^{-3} by changing the absorber layer thickness (0.1–0.9 μm). In an earlier report by Mahmoud *et al.* the efficiency improved with a defect density of 1×10^{14} cm^{-3}.[37] While an experimental verification by Noel

Open Access Article. Published on 28 November 2023. Downloaded on 11/13/2024 4:18:44 PM.
This article is licensed under a Creative Commons Attribution-NonCommercial 3.0 Unported Licence.

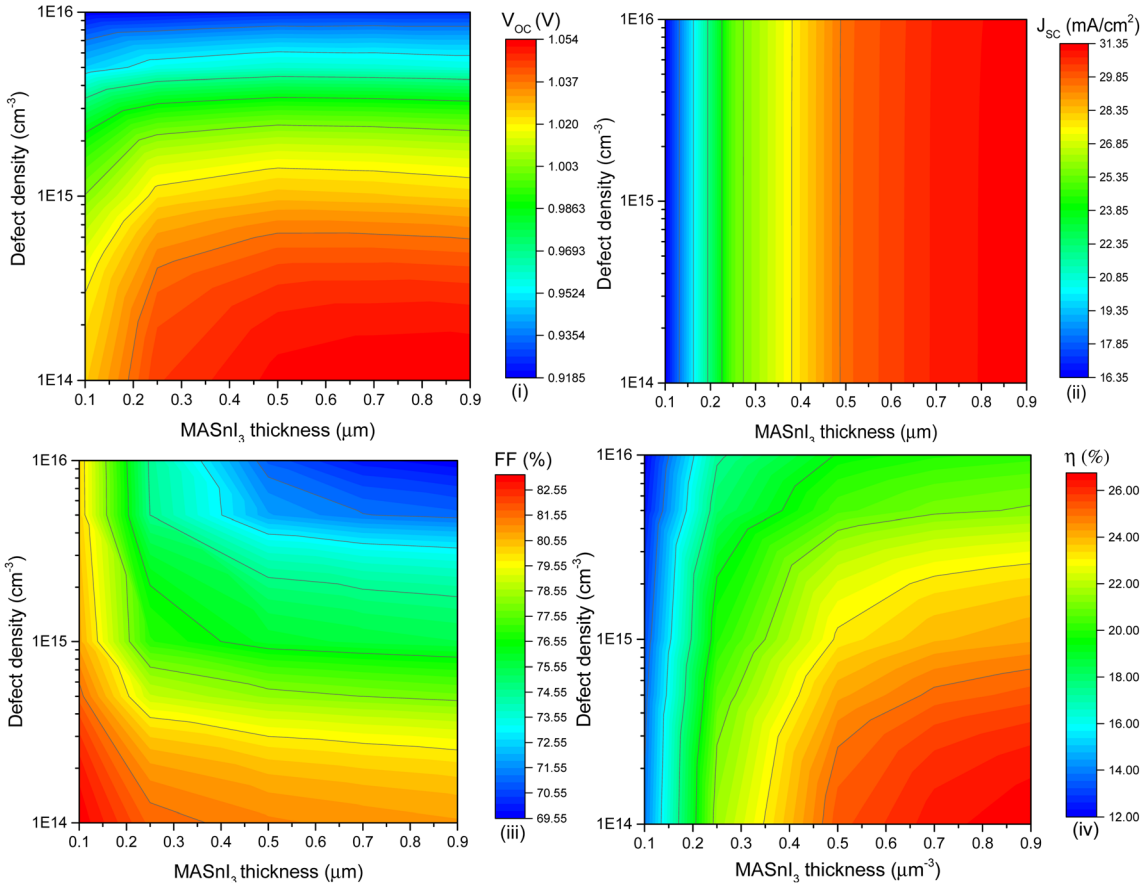

Fig. 8 The contour diagrams of simulated $MASnI_3$-PSC under optimized conditions with illuminance of AM1.5G.

et al. also depicted the same defect density in an $MASnI_3$-based PSC.[38]

4.5 The impact of acceptor density on the PSC parameters

The acceptor defect density varied between 1×10^{14} cm^{-3} and 5×10^{17} cm^{-3} and the corresponding PV parameters were obtained, as reported in Fig. 9. The disparity in the J_{SC} is well observed and achieves a maximum of 31.31 mA cm^{-2} at 1×10^{15} cm^{-3} and decreases to 29.8 mA cm^{-2}. In comparison, the V_{OC} and FF rise as the acceptor density increases. However, the PSC-device's relevant PCE was almost equal as the acceptor defect density varied from 1×10^{14} to 5×10^{17} cm^{-3}. So, the maximum PCE of 26.60% is presented at a smaller acceptor density (Fig. 9).

4.6 The influence of total defect density on four output parameters of the PSC

The most dominant solar cell output metrics (J_{SC}, V_{OC}, FF, and PCE) are presented in Fig. 10 as a function of defect density

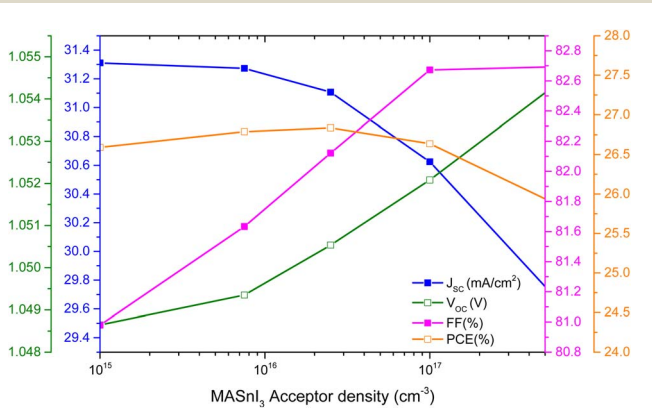

Fig. 9 The impact of $MASnI_3$ acceptor density on the PSC under illuminance of AM1.5G.

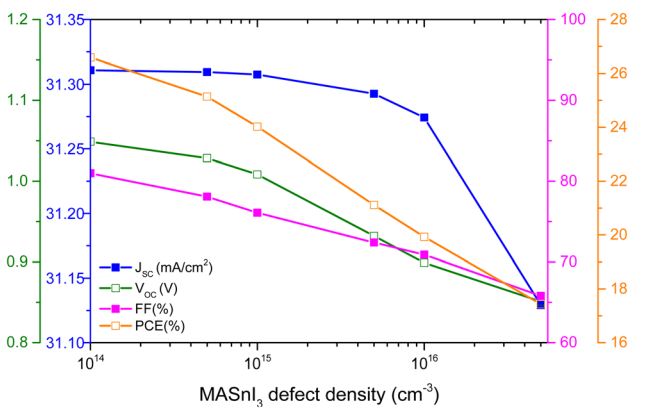

Fig. 10 The effect of $MASnI_3$ defect density on the PV outputs of the PSC devices.

© 2023 The Author(s). Published by the Royal Society of Chemistry

Open Access Article. Published on 28 November 2023. Downloaded on 11/13/2024 4:18:44 PM.
This article is licensed under a Creative Commons Attribution-NonCommercial 3.0 Unported Licence.

appertaining to the respective perovskite materials. Primarily, the PSC characteristics decrease as the defect density intensifies. It is crucial to note that the PSCs have drastically disparate solar cell parameter values. The $MASnI_3$-based perovskite efficiency is 26.60% at a defect density of 1×10^{14} cm^{-3}. The present result offers better outputs than the previous report by Dureja *et al.*[39] The $MASnI_3$-based PVK offers a high value of V_{OC}, *i.e.* almost 1.05 V. In addition, the architecture relevant to the device exhibits the same characteristics in terms of FF.

4.7 The impact of interface defect density on the output parameters of the PSCs

The study includes an investigation of $CuCrO_2/MASnI_3$ interface defect density. Fig. 11(i) shows the PCE over the defect density (N_t) pertaining to this interface. The calculation is concerned with the Fermi level relating to the device (E_F). As the PCE rises at smaller values of N_t (1×10^{10} cm^{-2}), the PCE is 26.60%. For further evaluation, the defect range from 1×10^{10} cm^{-2} to 1×10^{15} cm^{-2} was considered for further analysis. It was found that all four parameters are smaller for higher interface defect density ($N_t = 1 \times 10^{10}$ cm^{-2}). The $MASnI_3/CeO_2$ interface provides valuable information about the interface defect density between the PAL and the ETL layer, as depicted in Fig. 11(ii). Numerically, the maximum value of PCE is 26.60%, drastically dropping to 17.50% at $N_t = 1 \times 10^{15}$ cm^{-2}. It is emphasized that PCE is significantly affected, attributed to the higher level of N_t near the deep defect trap state.

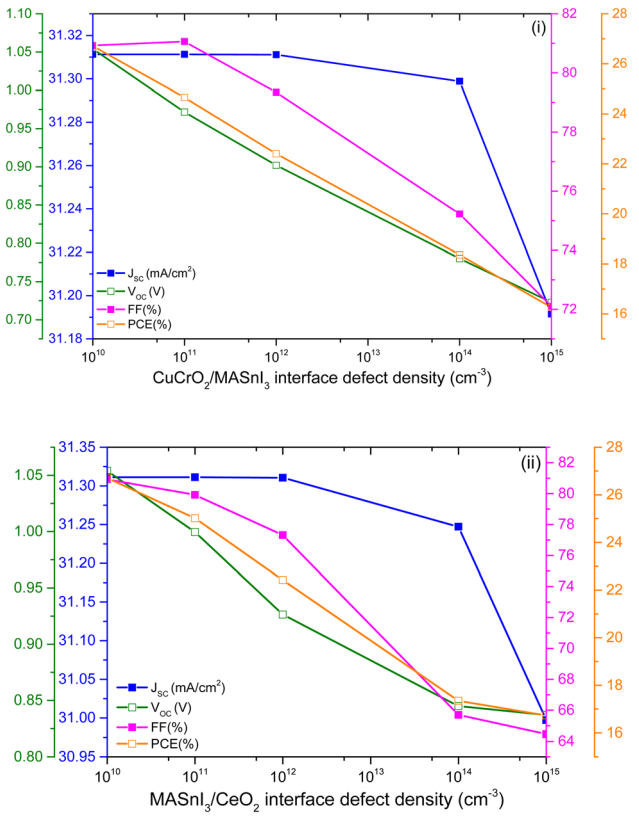

Fig. 11 (i and ii) The impact of both interfaces (L1 – $CuCrO_2/MASnI_3$ and L2 – $MASnI_3/CeO_2$) on the overall output of the PSC device.

4.8 The *J–V* characteristics of PSCs of different thicknesses, defect densities and temperatures

The *J–V* parameters pertaining to PSC devices for different ranges of thickness (100 nm to 900 nm), bulk defect density ($1 \times$

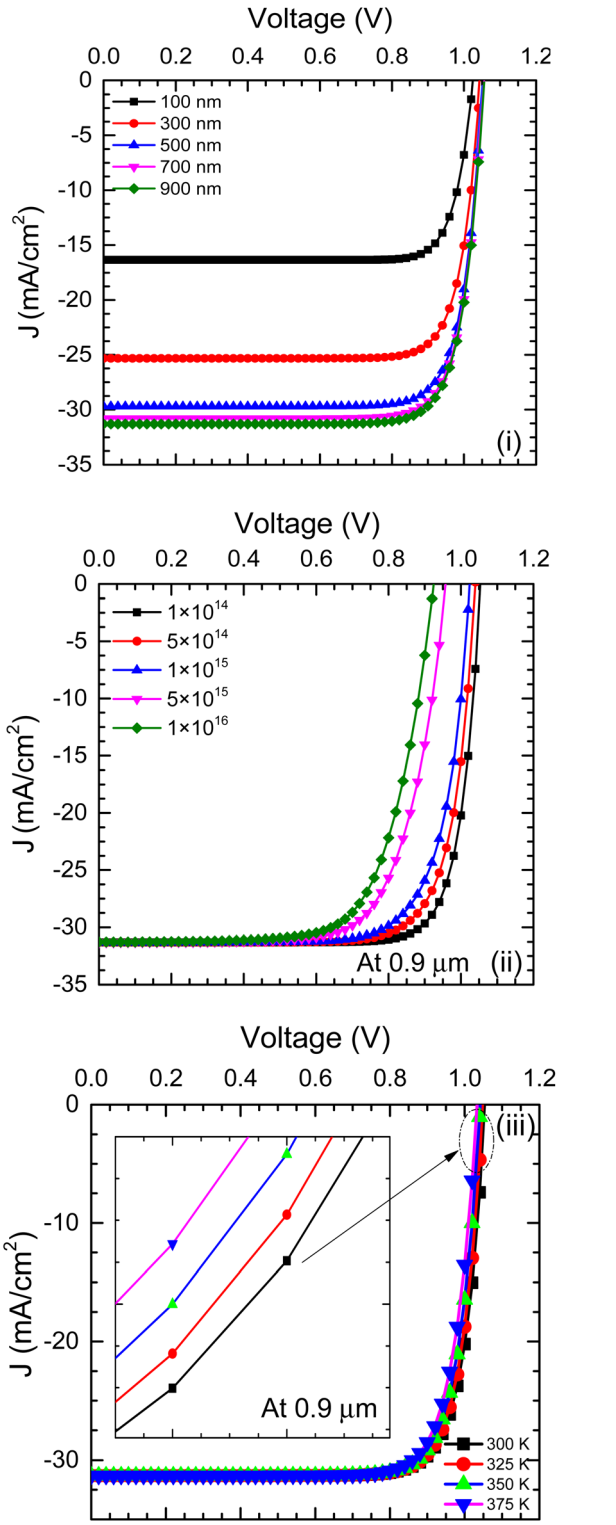

Fig. 12 Impact of (i) thickness, (ii) defect density, and (iii) temperature on the *J–V* parameter of the PSC devices.

Open Access Article. Published on 28 November 2023. Downloaded on 11/13/2024 4:18:44 PM.
This article is licensed under a Creative Commons Attribution-NonCommercial 3.0 Unported Licence.

10^{14} to 1×10^{16} cm^{-3}), and temperature (300–375 K) are depicted for a simulated PSC [Fig. 12(i–iii)]. Firstly, the current density intensifies as the thickness increases to attain a saturated value of 0.9 μm [Fig. 12(i)]. This may be due to extensive higher absorption with greater thickness. In Fig. 12(ii), increasing the defects greatly impacts the voltage and lowers the voltage when it achieves a value of 0.92 V at a higher defect density value. A comparable trend was noted for raising the temperature from 300 to 375 K, as depicted in Fig. 12(iii). The higher temperature lowers the V_{OC}, related to the damage done to the interior material of the PSC devices.[31,40] The $MASnI_3$-based PSC explicitly gives 1.05 V and 1.06 V at 300 and 375 K, respectively. The shift in potential from a higher to a lower value is well observed (Fig. 12).

4.9 The impedance, capacitance and EQE analysis of the optimized device

In the Nyquist curve, the *X*-axis represents resistance due to recombination, and the *Y*-axis represents the geometrical capacitance of the solar cell, indicating that the carrier accumulates at the interface layers. At high frequencies, the measured resistance resembles the recombination resistance of the material. The capacitance at high frequencies represents the geometric capacitance, signifying interface charge accumulation.[41] The low-frequency response is more dubious and is related to ionic motion and hysteresis.[42] It may turn into an inductive element due to the accumulation of ions and the reduction in extraction barriers. The study of imaginary and real impedance values can be well observed in Fig. 13. The impedance and real impedance show how reliable the device is, as a lower impedance is always preferable in PSC device manufacturing. The overall impedance value is -1.75×10^5 Ohm cm^2 with real impedance of 32 000 Ohm cm^2. Comparatively, the present work matches the value reported earlier by Bhattarai *et al.*[43]

A capacitance analysis for the PSC device provides an important outlook on the designed device. It can be seen that

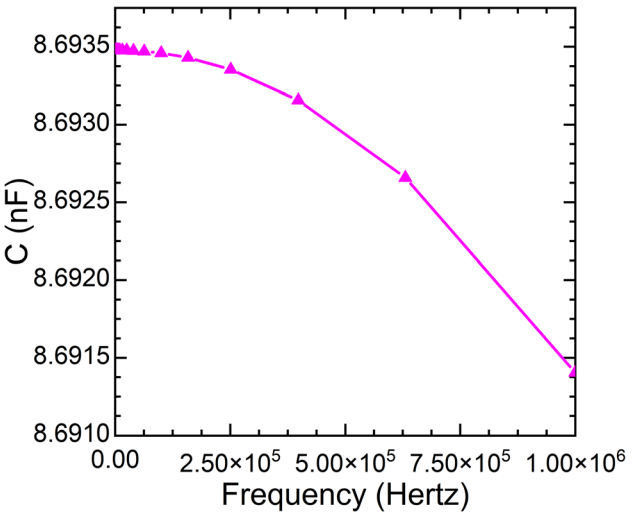

Fig. 14 Capacitance analysis of the designed PSC device after all-round optimization techniques.

the highest capacitance value is attained at a minimal level of defect density. The CF plot demonstrates that when the frequency surpasses 1 MHz, the capacitance reduces and saturates at a lower value. This behaviour could be attributed to specific physical processes occurring at different frequencies. The relatively smaller value of capacitance drops from nearly 8.6935 nF to 8.6915 nF in the frequency range of 10^6 Hertz, as depicted in Fig. 14. The capacitance of algal green-synthesized Au is much higher than the earlier reports from Bhattarai *et al.* for an $MASnI_3$-based PSC.[6]

For PSCs created with $MASnI_3$, the variation in QE with incident photon wavelength is presented in Fig. 15. The absorption of the perovskite materials can be understood with the help of the QE parameter of the PSC. The bandgap involving the absorbing layer presents an inverse relation with the QE

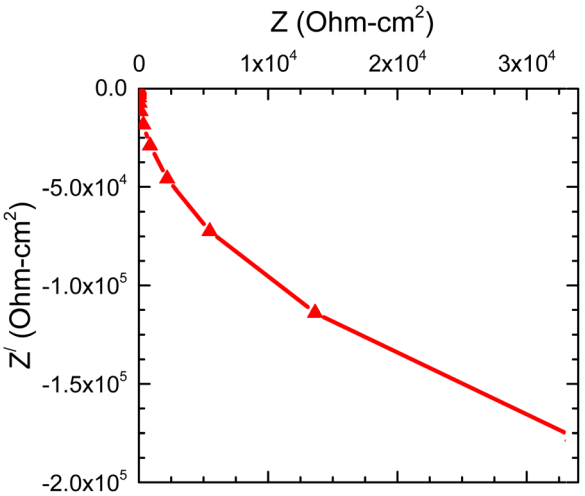

Fig. 13 Nyquist curve for the impedance analysis in the designed PSC device after all-round optimization techniques.

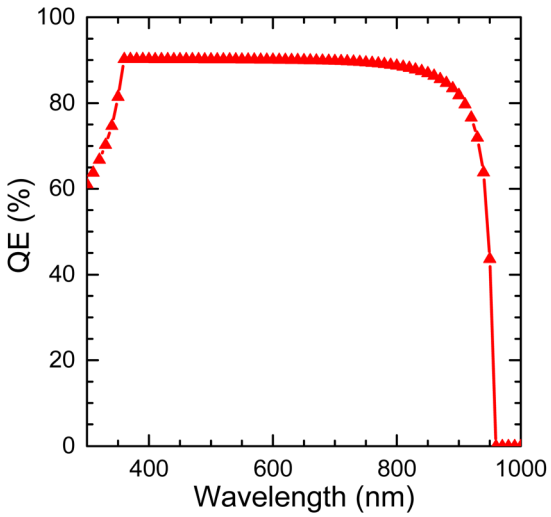

Fig. 15 Quantum efficiency (QE) with wavelength (nm) of the designed PSC device after all-round optimization techniques.

© 2023 The Author(s). Published by the Royal Society of Chemistry

Open Access Article. Published on 28 November 2023. Downloaded on 11/13/2024 4:18:44 PM.
This article is licensed under a Creative Commons Attribution-NonCommercial 3.0 Unported Licence.

Table 2 A comparison of the PV parameters of the simulated device with earlier work

Device structures	J_{SC} (mA cm^{-2})	V_{OC} (V)	FF (%)	PCE (%)
PSC device (present work)	31.31	1.05	80.98	26.60
Du *et al.*[44]	23.36	0.92	79.99	23.36
Singh *et al.*[45]	25.75	1.00	79.21	20.58
Alipour *et al.*[46]	24.65	1.12	86.02	23.69

pertinent to solar cells. The device absorbs wavelengths at varied ranges since $MASnI_3$ has a narrow bandgap (Fig. 15). Comparatively, the current relevant simulation of an $MASnI_3$-based PSC achieves an average QE of 90%, which is reasonably more optimised than the report mentioned above by Bhattarai *et al.*[31] Apart from that, a detailed comparison with earlier works is given in Table 2.

5. Conclusions

In conclusion, the most critical solar cell attributes were analysed using the carrier transport approach in the green-synthesized carrier transport layer with reference to $MASnI_3$-based PSC devices, and the most critical solar cell attributes were analysed. The electric parameter is predicted to be significantly more affected by the active layer appertaining to the PSC designs than by the carrier transport layers (CTLs). Therefore, PAL has been optimized for the simulated device. We obtained an appropriate active layer thickness (0.9 μm) for an $MASnI_3$-based PSC. The green-synthesized HTL and ETL, $CuCrO_2$ and CeO_2, also improved the efficiency of the PSC device. Additionally, algae-synthesized Au nanoparticles are used as the back contact, notably being very productive so far as the cost and the overall development of the device are concerned. The capacitance and impedance analysis (imaginary *vs.* real *Z*) were also performed for the device architectures appertaining to the doping conditions to assess the dependence of the PSC device on the $MASnI_3$ materials. The optimized PSC device achieves an excellent PCE of 26.60% for device fabrication. The study also provides a critical recommendation as well as a demonstration to help in the effective manufacturing of an $MASnI_3$-based PSC.

Conflicts of interest

There are no conflicts to declare.

Acknowledgements

The authors would like to express their sincere gratitude to Dr Marc Burgelman and his staff at the University of Gent Belgium for providing the open-source SCAPS-1D simulation software.

References

1 H. J. Snaith, Perovskites: The Emergence of a New Era for Low-Cost, High-Efficiency Solar Cells, *J. Phys. Chem. Lett.*, 2013, **4**(21), 3623–3630.
2 H.-S. Kim, S. H. Im and N.-G. Park, Organolead Halide Perovskite: New Horizons in Solar Cell Research, *J. Phys. Chem. C*, 2014, **118**(11), 5615–5625.
3 J. M. Ball, *et al.*, Optical properties and limiting photocurrent of thin-film perovskite solar cells, *Energy Environ. Sci.*, 2015, **8**(2), 602–609.
4 S. Rhee, K. An and K.-T. Kang, Recent Advances and Challenges in Halide Perovskite Crystals in Optoelectronic Devices from Solar Cells to Other Applications, *Crystals*, 2021, **11**, DOI: 10.3390/cryst11010039.
5 M. I. H. Ansari, A. Qurashi and M. K. Nazeeruddin, Frontiers, opportunities, and challenges in perovskite solar cells: A critical review, *J. Photochem. Photobiol., C*, 2018, **35**, 1–24.
6 S. Bhattarai, *et al.*, Performance improvement approach of all inorganic perovskite solar cell with numerical simulation, *Mater. Today Commun.*, 2022, **33**, 104364.
7 S. Bhattarai, *et al.*, Numerical Simulation to Design an Efficient Perovskite Solar Cell Through Triple-Graded Approach, *J. Electron. Mater.*, 2021, **50**(12), 6756–6765.
8 S. Bhattarai, *et al.*, Numerical simulation study for efficiency enhancement of doubly graded perovskite solar cell, *Opt. Mater.*, 2021, **118**, 111285.
9 A. Kojima, *et al.*, Organometal Halide Perovskites as Visible-Light Sensitizers for Photovoltaic Cells, *J. Am. Chem. Soc.*, 2009, **131**(17), 6050–6051.
10 M. K. Hossain, *et al.*, Numerical Analysis in DFT and SCAPS-1D on the Influence of Different Charge Transport Layers of CsPbBr3 Perovskite Solar Cells, *Energy Fuels*, 2023, **37**(8), 6078–6098.
11 B. Rivkin, *et al.*, Effect of Ion Migration-Induced Electrode Degradation on the Operational Stability of Perovskite Solar Cells, *ACS Omega*, 2018, **3**(8), 10042–10047.
12 K. Kranthiraja, *et al.*, Stability and degradation in triple cation and methyl ammonium lead iodide perovskite solar cells mediated via Au and Ag electrodes, *Sci. Rep.*, 2022, **12**(1), 18574.
13 D. Wei, *et al.*, Photo-induced degradation of lead halide perovskite solar cells caused by the hole transport layer/metal electrode interface, *J. Mater. Chem. A*, 2016, **4**(5), 1991–1998.
14 H.-S. Kim, *et al.*, Lead Iodide Perovskite Sensitized All-Solid-State Submicron Thin Film Mesoscopic Solar Cell with Efficiency Exceeding 9%, *Sci. Rep.*, 2012, **2**(1), 591.
15 D. Liu and T. L. Kelly, Perovskite solar cells with a planar heterojunction structure prepared using room-temperature solution processing techniques, *Nat. Photonics*, 2014, **8**(2), 133–138.
16 A. Singla, *et al.*, Numerical Simulation of CeOx ETL based Perovskite Solar Cell: An Optimization Study for High Efficiency and Stability, in *2018 IEEE Electron Devices Kolkata Conference*, EDKCON, 2018.
17 J. Chen, *et al.*, Effect of bidentate and tridentate additives on the photovoltaic performance and stability of perovskite solar cells, *J. Mater. Chem. A*, 2019, **7**(9), 4977–4987.
18 D. Muchahary, *et al.*, Heterojunction between crystalline silicon and nanocomposite coupled ZnO·SnO2 and

Open Access Article. Published on 28 November 2023. Downloaded on 11/13/2024 4:18:44 PM. This article is licensed under a Creative Commons Attribution-NonCommercial 3.0 Unported Licence.

optimization of its photovoltaic performance, *Curr. Appl. Phys.*, 2022, **38**, 15–21.
19 A. Butt, *et al.*, Biogenic synthesis of cerium oxide nanoparticles using petals of *Cassia glauca* and evaluation of antimicrobial, enzyme inhibition, antioxidant, and nanozyme activities, *Biochem. Syst. Ecol.*, 2022, **104**, 104462.
20 D. Sarkar, A comprehensive study on $RbGeI_3$ Based Inorganic Perovskite Solar Cell Using Green Synthesized $CuCrO_2$ as hole conductor, *J. Photochem. Photobiol., A*, 2023, **439**, 1146231.
21 B. Sharma, *et al.*, Biosynthesis of gold nanoparticles using a freshwater green alga, Prasiola crispa, *Mater. Lett.*, 2014, **116**, 94–97.
22 A. Hima, *et al.*, An optimized perovskite solar cell designs for high conversion efficiency, *Superlattices Microstruct.*, 2019, **129**, 240–246.
23 C. Devi and R. Mehra, Device simulation of lead-free MASnI3 solar cell with CuSbS2 (copper antimony sulfide), *J. Mater. Sci.*, 2019, **54**(7), 5615–5624.
24 S. Rawat, R. Gupta and S. Gohri, Performance assessment of CIGS solar cell with different CIGS grading profile, *Mater. Today: Proc.*, 2023, DOI: **10.1016/j.matpr.2023.03.356**.
25 S. Bhattarai, *et al.*, Numerical investigation of toxic free perovskite solar cells for achieving high efficiency, *Mater. Today Commun.*, 2023, **35**, 105893.
26 S. Bhattarai, Numerical simulation study for efficiency enhancement of doubly graded perovskite solar cell, *Opt. Mater.*, 2021, **118**, 111285.
27 M. Burgelman, *et al.*, Modeling thin-film PV devices, *Prog. Photovoltaics*, 2004, **12**, 143–153.
28 M. Burgelman and J. Marlein, Analysis of graded band gap solar cells with SCAPS, *Proceedings of the 23rd European Photovoltaic Conference*, 2008.
29 J. Madan, *et al.*, Device simulation of 17.3% efficient lead-free all-perovskite tandem solar cell, *Sol. Energy*, 2020, **197**, 212–221.
30 S. Abdelaziz, *et al.*, Investigating the performance of formamidinium tin-based perovskite solar cell by SCAPS device simulation, *Opt. Mater.*, 2020, **101**, 109738.
31 S. Bhattarai, *et al.*, Investigation of Carrier Transport Materials for Performance Assessment of Lead-Free Perovskite Solar Cells, *IEEE Trans. Electron Devices*, 2022, **69**(6), 3217–3224.
32 S. Ahmmed, *et al.*, Performance analysis of lead-free CsBi3I10-based perovskite solar cell through the numerical calculation, *Sol. Energy*, 2021, **226**, 54–63.
33 S. Jeong, S. Seo and H. Shin, p-Type CuCrO2 particulate films as the hole transporting layer for CH3NH3PbI3 perovskite solar cells, *RSC Adv.*, 2018, **8**(49), 27956–27962.
34 S. Bhattarai, A. Sharma and T. D. Das, Factor affecting the performance of perovskite solar cell for distinct MAPI layer thickness, *AIP Conf. Proc.*, 2020, **2269**(1), 030071.
35 S. Bhattarai and T. D. Das, Optimization of carrier transport materials for the performance enhancement of the MAGeI3 based perovskite solar cell, *Sol. Energy*, 2021, **217**, 200–207.
36 S. Bhattarai, *et al.*, Performance analysis and optimization of all-inorganic CsPbI3-based perovskite solar cell, *Indian J. Phys.*, 2023, **97**, 2629–2637.
37 K. H. Mahmoud, *et al.*, Comparative Analysis of Perovskite Solar Cells for Obtaining a Higher Efficiency Using a Numerical Approach, *Micromachines*, 2023, **14**(6), 1127.
38 N. K. Noel, *et al.*, Lead-free organic–inorganic tin halide perovskites for photovoltaic applications, *Energy Environ. Sci.*, 2014, **7**(9), 3061–3068.
39 T. Dureja, *et al.*, Double lead-free perovskite solar cell for 19.9% conversion efficiency: a SCAPS-1D based simulation study, *Mater. Today: Proc.*, 2022, **71**, 239–242.
40 A. Thakur, D. Singh and S. Kaur Gill, Numerical simulations of 26.11% efficient planar CH3NH3PbI3 perovskite n-i-p solar cell, *Mater. Today: Proc.*, 2022, **71**, 195–201.
41 E. von Hauff and D. Klotz, Impedance spectroscopy for perovskite solar cells: characterisation, analysis, and diagnosis, *J. Mater. Chem. C*, 2022, **10**(2), 742–761.
42 A. Guerrero, J. Bisquert and G. Garcia-Belmonte, Impedance Spectroscopy of Metal Halide Perovskite Solar Cells from the Perspective of Equivalent Circuits, *Chem. Rev.*, 2021, **121**(23), 14430–14484.
43 S. Bhattarai, A. Sharma and T. D. Das, Efficiency enhancement of perovskite solar cell by using doubly carrier transport layers with a distinct bandgap of MAPbI3 active layer, *Optik*, 2020, **224**, 165430.
44 H.-J. Du, W.-C. Wang and J.-Z. Zhu, Device simulation of lead-free CH3NH3SnI3 perovskite solar cells with high efficiency, *Chin. Phys. B*, 2016, **25**(10), 108802.
45 N. Singh, Numerical simulation of highly efficient lead-free perovskite layers for the application of all-perovskite multi-junction solar cell, *Superlattices Microstruct.*, 2021, **149**, 106750.
46 H. Alipour and A. Ghadimi, Optimization of lead-free perovskite solar cells in normal-structure with WO3 and water-free PEDOT: PSS composite for hole transport layer by SCAPS-1D simulation, *Opt. Mater.*, 2021, **120**, 111432.

© 2023 The Author(s). Published by the Royal Society of Chemistry